Development of a Surface Charging Assessment System for the GEO Region by Combining Global Magnetosphere MHD and Spacecraft Charging Models

Aoi Nakamizo [ID], Masao Nakamura, Tsutomu Nagatsuma [ID], Yasubumi Kubota [ID], Kiyokazu Koga, Haruhisa Matsumoto [ID], and Yoshizumi Miyoshi [ID], *Member, IEEE*

Abstract— For the safety and stability of satellite operations, we have been conducting a satellite charging estimation project, Space Environment Customized Risk Estimation for Satellites (SECURES), by linking space environment models and spacecraft charging models. In SECURES-Surface Charging, we use the global magnetosphere MHD model as the environment model and target the geostationary orbit (GEO) region as the first step of the surface charging estimation. To perform the magnetosphere simulation under realistic conditions, we improved the model by introducing the effects of the tilt and precession of the Earth's dipole axis. By comparing the simulation data of the improved magnetosphere MHD model and observation data for the GEO region, we found that the simulated pressure is in good agreement with the observed electron pressure. However, the simulated density is much higher than the observed electron density, and the simulated temperature is lower than the observed electron temperature. Utilizing these characteristics, we developed a method of estimating the input parameters for spacecraft charging models from the magnetosphere MHD simulation output. As for the satellite surface charging calculation, we developed a method of estimating instantaneously the equilibrium surface potentials based on the precalculation analysis using the spacecraft plasma interaction system (SPIS). Based on these two methods, we developed a surface charging assessment system for a model satellite in the GEO region (https://secures.nict.go.jp), which operates in real time by combining the global magnetosphere MHD model and SPIS.

Index Terms— Magnetosphere, modeling, simulation, surface charging.

I. Introduction

ELECTROSTATIC discharge (ESD) is one of the major causes of satellite anomalies (see [1], [2]). There are two charging mechanisms that lead to ESD, namely, the surface charging caused by keV-order particles and the internal charging caused by high-energy (>MeV-order) plasmas. The plasma environment is different depending on the satellite location. In addition, how severely a satellite is charged in a certain plasma environment depends on the design and material of the satellite itself. Therefore, it is difficult to assess the charging risk of a satellite from the general space weather information. Therefore, for the safety and stability of satellite operations, we have been conducting a charging risk estimation project, Space Environment Customized Risk Estimation for Satellites (SECURES) [3].

Our approach in SECURES is as follows. We combine space environment simulation models, which specify the plasma environment, and spacecraft charging models, which calculate, for given plasma data, the charging status of a model spacecraft predesigned with information on the shape and materials of the spacecraft. (We are presently using the spacecraft plasma interaction system (SPIS) [4] and multiutility spacecraft charging analysis tool (MUSCAT) [5], [6].) We extract plasma data from the simulated space environment along an orbit of an individual satellite and calculate a charging status by inputting the extracted data into the satellite model. In this way, we assess the charging risk of individual satellites. In this article, we present the activity of SECURES-Surface Charging and its achievement.

Since 1970, it has been known that the occurrence of surface charging is well-correlated with magnetospheric substorm activities. DeForest [7] showed that a geostationary orbiting satellite ATS-5 located in the nightside eclipse region was severely charged (up to −9000 V) due to 1–10-keV plasma injections associated with substorms. Spence et al. [8] showed that the surface charging of high-inclination, high-latitude satellites was related to 10–15-keV plasma injections during

substorms. Subsequent studies (see [9], [10], [11]) showed that the occurrence of surface charging events is distributed from around midnight, where substorm injection occurs, to early morning sectors. From these numerous previous studies, it has been widely accepted that the main cause of surface charging is the hot (several–several tens of keV) plasmas injected from the nightside plasma sheet in association with substorms.

The geostationary orbit (GEO) is one of the regions where a very large number of satellites, including those maintaining social infrastructures, are in operation. The nightside GEO is also the region exposed to substorm plasma injection, which induces surface charging. Therefore, in our SECURES-Surface Charging Project, we target the nightside GEO region for surface charging estimation as a first step.

Due to the concerns about surface charging, numerous studies on the GEO plasma environment have been conducted. Those studies target, for example, the relationships among the GEO plasma environment, magnetospheric activities, and the solar cycle (see [12], [13]); the plasma environment leading to surface charging and its solar cycle, seasonal, and local time (LT) dependences [14]; and its dependences on the solar wind/interplanetary magnetic field (IMF) parameters and geomagnetic indices [15]. Moreover, empirical models based on observational data analysis have been proposed (see [16], [17]). Physics-based models, such as inner magnetosphere models (see [18], [19], [20], [21]) and global magnetosphere MHD models (see [22], [23], [24], [25], [26]), can be used to infer the plasma environment in the near-Earth space including the GEO region. In recent years, further improvements in these physics-based models and the model couplings targeting surface charging have been made (see [27], [28], [29], [30]). For earlier models, both the empirical and physics-based models are summarized in [31].

As our environment model, we use a global magnetosphere MHD model [32]. The global magnetosphere MHD model is powerful in that it solves, as a stand-alone, the solar wind–magnetosphere–ionosphere system in a first principle and describes the magnetospheric substorm activities. As the spacecraft charging model, we use SPIS [4]. We construct a geometrical model of the target satellite in SPIS and calculate the surface potentials of the satellite by inputting the plasma environment data simulated by the magnetosphere MHD model. In this way, based on physics-based models for both the geospace environment and the satellite charging, we aim to provide surface charging information tailored to individual satellites, rather than general environmental information or general surface charging information.

In the following, we show the outline and improvement of the magnetosphere MHD model, the setting of a model satellite using SPIS, two challenges in combining the magnetosphere MHD model output and the charging calculation by SPIS, and our first product. Finally, we discuss the limitations and achievements of this study.

II. GLOBAL MAGNETOSPHERE MHD MODEL

We use the global magnetosphere MHD model originally developed in [33]. The first version of the computational grid system was based on a modified polar coordinate system.

To simulate global systems including fine structures in their center with sufficiently high spatial resolution and numerical stability, the grid system was upgraded to a triangular unstructured grid system [34], [35], [36]. Recently, the message passing interface (MPI) parallelized version, called REPPU, has been developed in [32].

The model solves an MHD equation system written by describing the magnetic field $\mathbf{B}$ as $\mathbf{B} = \mathbf{B_0} + \mathbf{B_1}$, where $\mathbf{B_0}$ is the Earth's dipole field and $\mathbf{B_1}$ is the perturbation component from $\mathbf{B_0}$ [33]. The model includes a 2-D ionospheric solver at the inner boundary. The main equation is the following Poisson equation derived from the ionospheric Ohm's law and the equality between the current divergence of the 2-D approximated ionosphere and the field-aligned currents (FACs) flowing between the magnetosphere and the ionosphere:

$$\nabla \cdot [\Sigma \cdot (\nabla \Phi)] = -j_{||} \tag{1}$$

$$\mathbf{E} = -\nabla \Phi \tag{2}$$

where Σ is the ionospheric conductance tensor, Φ is the electrostatic potential, $j_{||}$ is the FAC density mapped to the ionospheric altitude ($1 R_{\mathrm{E}}$) from that calculated by $\nabla \times \mathbf{B_1}$ at the inner boundary (placed at $2.6 \sim 3 R_{\mathrm{E}}$), and $\mathbf{E}$ is the electric field. Here, $j_{||}$ is defined as positive and negative for downward and upward FACs, respectively. The obtained $\mathbf{E}$ is mapped back to the inner boundary, and the perpendicular component of the bulk velocity in the magnetosphere is updated by $\mathbf{V}_{\perp} = (-\mathbf{E} \times \mathbf{B})/B^2$.

Ionization is caused by solar extreme ultraviolet (EUV) rays and particle precipitation from the magnetosphere. The contribution of the former to conductance is calculated as a function of the solar zenith angle (SZA) and F10.7 index. The contribution of the latter to conductance is calculated as a function of thermal pressure and temperature at the inner boundary (corresponding to diffuse precipitation) and a function of the upward FAC density (corresponding to discrete precipitation). The simulation is driven by inputting the solar wind parameters (velocity, density, and thermal pressure) and IMF at the upstream of the magnetosphere in the model.

III. IMPROVEMENT OF MAGNETOSPHERE MHD MODEL FOR OPERATIONAL USES

The Earth's rotation axis is tilted with respect to the ecliptic plane, and the magnetic dipole axis is tilted from the rotation axis, resulting in precession, which causes, for example, the seasonal variation of magnetosphere–ionosphere disturbances. However, the original model, as in the case of other models, does not include the tilt and precession of the dipole axis for simplicity. For performing simulations under realistic conditions, this point has been a long-lasting issue of the original model [37]. On the other hand, the computation should not be slowed down for operational uses.

To simultaneously resolve these two issues, we carry out the coordinate transformation of the vector quantities of external input parameters (solar wind velocity and IMF) and the distribution of the solar EUV-dependent component of ionospheric conductance. Specifically, we adopt the solar magnetic (SM) coordinate system for the simulation. We transform solar wind

This article has been accepted for inclusion in a future issue of this journal. Content is final as presented, with the exception of pagination.

NAKAMIZO et al.: DEVELOPMENT OF A SURFACE CHARGING ASSESSMENT SYSTEM FOR THE GEO REGION
3

TABLE I

MATERIAL PROPERTIES OF THE MICHIBIKI-1 SATELLITE (ADAPTED FROM [42])

Surface material	Thickness (m)	Photoemission Current (Am^{-2})	Electron Yield	Electron Max (keV)	Proton Yield	Proton Max (keV)	Bulk Conductivity $(\Omega^{-1}m^{-1})$	Dielectric Constant
Cover Glass	1.0E-04	1.5E-05	3.3	0.8	0.244	230	1.0E-16	4
Black Kapton	2.54E-05	7.2E-06	0.93	0.28	0.455	140	-1*	3.5
SiO$_2$	1.27E-04	2.0E-05	2.4	0.4	0.244	230	1.0E-14	4
ITO+OSR	1.0E-6	1.5E-05	1.4	0.8	0.49	123	-1*	1*
Aluminum	1.0E-3	4.0E-05	0.97	0.3	0.244	230	-1*	1*
CFRP	2.0E-4	4.0E-06	2.1	0.15	0.413	135	-1*	4.3

*Dielectric Constant = 1 and Conductance = -1 mean that the material is considered as a conductor in the simulation.
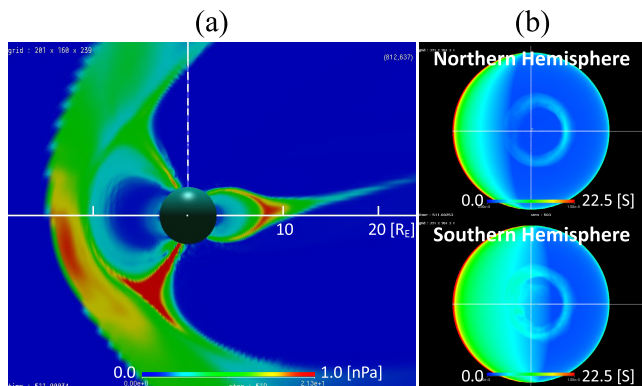

Fig. 1. Snapshot of the magnetosphere and ionosphere under a winter eclipse condition simulated using the improved magnetosphere MHD model. (a) Thermal pressure distribution in the magnetosphere. (b) Ionospheric conductance distributions in the northern and southern hemispheres.

velocity and IMF, which are generally given in the geocentric solar ecliptic (GSE) or geocentric solar magnetospheric (GSM) coordinate system, into the SM coordinate system. In addition, we calculate the distribution of the solar EUV-dependent component of ionospheric conductance in the SM coordinate system. These modifications are executed at every time step of the simulation. In this way, we equivalently include the tilt and precession of the dipole axis in the simulation.

A simulation result for the transformed solar wind and IMF input is shown in [38]. The initial result for simulation with both the solar wind and IMF transformation and ionospheric conductance transformation, that is, the result including completely the effects of tilt and precession, is reported in [39]. Fig. 1 shows a snapshot of the magnetosphere and ionosphere under a winter eclipse condition simulated using the improved model. Due to the improvements made in [38], the simulated magnetosphere is elevated from the equatorial plane of the SM coordinate system because, in the winter season, the solar wind has the $+Z$ component in the SM coordinate system. Due to the improvements made in [39], in addition to the modification of the solar wind and IMF directions, the distributions of the ionospheric background (solar EUV-dependent) conductance in the northern and southern hemispheres are adjusted to the winter and summer conditions, respectively.

In parallel with these improvements, we developed a real-time simulation system on the high-performance computing (HPC) system at the National Institute of Information and Communications Technology (NICT) [40]. The simulation is driven by the real-time solar wind and IMF data observed at the L1 point of the Sun–Earth system provided by the National Oceanic and Atmospheric Administration's Space Weather Prediction Center (NOAA/SWPC). Since mid-August 2020, the real-time simulation fully including the effects of the tilt and precession of the dipole axis has been operational.

IV. SPACECRAFT CHARGING MODEL AND MODEL SATELLITE

For the calculation of the surface charging of individual satellites, we use SPIS [4], one of the spacecraft charging models. SPIS calculates the development of surface potentials for a predesigned spacecraft model with the input of environment data under the sunlit or eclipse condition. SPIS assumes that the ambient plasma is in a single-Maxwellian or double-Maxwellian distribution. Therefore, the input parameters are representative values of the densities and temperatures of electrons and ions (Ne, Ni, Te, and Ti) for the single-Maxwellian assumption and two representative values of them for the double-Maxwellian assumption.

As a model satellite in our present charging estimation, we set the Michibiki-1 satellite, a typical three-axis stabilized geosynchronous satellite with dielectric materials [41], assuming a Japanese commercial satellite. Fig. 2 shows the geometry of the Michibiki-1 satellite built on SPIS, and Table I shows the details of the surface materials [42]. For this model satellite, we calculate the floating potentials of the surface materials in equilibrium, for a given plasma environment dataset.

Fig. 3 shows the computational domain and mesh grids on the surfaces of the model satellite. (Adapted from [42].) The computational domain has two boundaries: the inner and outer boundaries. The inner rectangular boundary is $6 \times 30 \times 12$ [m] with dense meshes and the outer spheroidal boundary is 60×36 [m] with sparse meshes. The mesh resolution of the MHD model is the finest in the midnight equatorial region. For the GEO region, the finest resolution is approximately 0.165, 0.210, and 0.130 [R_E] (R_E: Earth's radius) for the radial, azimuthal, and latitudinal directions, respectively. Therefore, the SPIS computational domain is much smaller than one cell of the MHD model. As noted in the Introduction and subsequent sections, we extract the plasma data at the satellite location from the magnetosphere MHD simulation and use them as the input of SPIS. The

This article has been accepted for inclusion in a future issue of this journal. Content is final as presented, with the exception of pagination.

4   IEEE TRANSACTIONS ON PLASMA SCIENCE
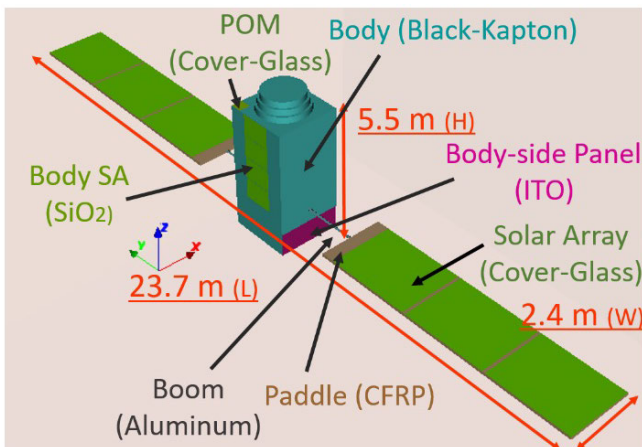

Fig. 2. Geometry of the Michibiki-1 satellite built on SPIS. (Adapted from [42]).
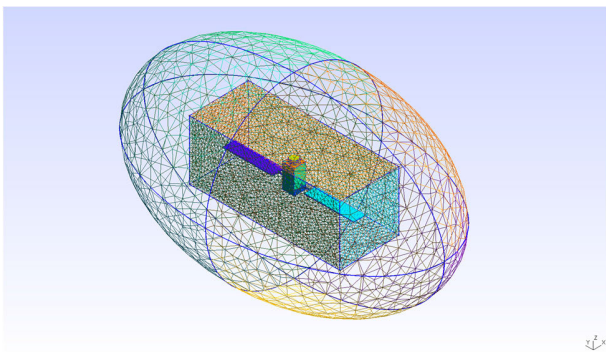

Fig. 3. Computational domain and mesh grids on the surfaces of the model satellite. (Adapted from [42]).

plasma environment data at the satellite location at a certain time are obtained by finding a computational cell that contains the satellite location and supplementing it with the data at the grid points that make up the cell. We perform the charging calculation with the default SPIS GEO setting. For details, see "SPIS User Manual" and "SPIS User Manual—Annex 1—Spacecraft Surface Charging in GEO/MEO" (https://www.spis.org/software/spis/documentation).

By using NASCAP-2k and MUSCAT, Toyoda and Ferguson [43] performed a round-robin simulation of the surface charging of an assumed generic GEO satellite for severe plasma environment data observed in the past. Nakamura et al. [44] performed the same round-robin simulation by using SPIS. Our method of constructing the model satellite and its charging calculations shown below is the same as that in [44]. Therefore, although the satellite model used in this study and that used in [43] and [44] are different, our charging calculation is reasonable.

V. Two Challenges for SECURES-Surface Charging

The magnetosphere MHD model is ready for operational use and the surface charging calculation for a model satellite by the spacecraft charging model (here, we use SPIS) is also ready. However, we have the following two challenges in combining the magnetosphere MHD model and the spacecraft charging model

Challenge 1: The spacecraft charging models require the densities and temperatures of electrons and ions as their input. However, in general, MHD models do not provide the electron and ion parameters separately. Therefore, the magnetosphere MHD simulation output cannot be used directly as the input of the spacecraft charging models.

Challenge 2: The charging calculation by the spacecraft charging models usually takes hours or days for one space environment condition. For the space environment data that changes from moment to moment, we need to obtain the calculation results in a short time.

We took the following approach to overcome these challenges, targeting the GEO region as the first step. For challenge 1, we developed a method of estimating one representative value for each of the densities and temperatures of electrons and ions (Ne, Ni, Te, and Ti) from the MHD simulation output, assuming a single-Maxwellian distribution. For challenge 2, we developed a method of quickly estimating the equilibrium surface potential for a given environment data by using SPIS. We describe the details in the next sections.

VI. Estimation of Input Parameters of Spacecraft Charging Model From Magnetosphere MHD Simulation Output

Nagatsuma et al. [3] developed a method of estimating Ne, Ni, Te, and Ti from the MHD simulation output by comparing the data of the magnetospheric plasma analyzer (MPA) onboard Los Alamos National Laboratory (LANL) satellites (provided by CDAWeb (https://cdaweb.gsfc.nasa.gov) and simulation data). Details are as follows.

1) We refer to [45] that showed that the simulated MHD pressure P_{SIM} in the nightside GEO region has good correlation with the observed electron pressure Pe.
2) From February to April 2006, we selected events in which LANL/MPA observed negative satellite potential during substorms while the satellites were on the nightside.
3) For the selected events, we performed MHD simulations using the spacecraft-interspersed, near-Earth solar wind data (OMNI) solar wind and IMF data (provided by CDAWeb (https://cdaweb.gsfc.nasa.gov) as the input.
4) We extracted the time-series simulation data along the LANL satellite orbits and then compared them with the MPA data. The simulated pressure P_{SIM} in the nightside GEO region has good correlation with the observed electron pressure Pe, similar to the result in [45].
5) We focus on the data when Pe peaked, leading to negative charging. For each event, we searched for the P_{SIM} peak within ±30 min from the Pe peak, then compared the simulation and observational data at each pressure peak.
6) P_{SIM} has good correlation with Pe. On the other hand, the simulated density N_{SIM} tends to be much higher than Ne, which is almost about 1.0 [cm^{-3}], and the simulated temperature T_{SIM} tends to be lower than Te.
7) From the results, we estimate the electron temperature from P_{SIM} assuming Ne = 1.0 [cm^{-3}]. We define the electron temperature estimated in this way as T_{SIM-e}. For

This article has been accepted for inclusion in a future issue of this journal. Content is final as presented, with the exception of pagination.

NAKAMIZO et al.: DEVELOPMENT OF A SURFACE CHARGING ASSESSMENT SYSTEM FOR THE GEO REGION 5

the ion temperature, we multiply T_{SIM-e} by the average ratio of Ti–Te, which is about 1.9. We define the ion temperature estimated in this way as T_{SIM-i}.

In summary, we estimate the input of spacecraft charging models from the simulation output as follows:

$$N_e = N_p = 1.0 \tag{3}$$

$$T_{SIM-e} = P_{SIM}/(k_B \times N_e) \tag{4}$$

$$T_{SIM-i} = 1.9 \times T_{SIM-e} \tag{5}$$

where k_B is Boltzmann's constant.

Between the simulation code set used in the previous analysis and that currently used in the real-time simulation, the details of the model settings are different at some points (e.g., the spatial resolution of the computational grid and coefficients in the ionospheric conductance setting). In the following, we check the above estimation method using a simulation code set with exactly the same model setting as that currently used in real-time simulation.

Fig. 4(a)–(d) shows the OMNI data, namely, IMF, solar wind speed, solar wind density, and auroral upper (AU)/auroral lower (AL) indices, respectively. Fig. 4(e)–(i) shows the LANL(L4)/MPA data, namely, satellite potential, electron and ion densities (Ne and Ni), temperatures (Te and Ti), thermal pressures (Pe and Pi), and satellite orbit, respectively. The electron and ion data are shown as red and blue lines, respectively.

The LANL/MPA data show a severe negative charging during 10:00–11:30 UT in association with the enhancement of Pe and Te. The enhancement is likely related to a substorm occurring around 10:00 UT as shown by the AL index.

The simulation data are plotted as magenta lines in Fig. 4(d) and (f)–(h). It can be seen from Fig. 4(d) that the magnetosphere simulation well-reproduced the magnetospheric substorm activity. As for the GEO region, whereas N_{SIM} is much higher than Ne and Ni, P_{SIM} well traces Pe, similar to the result of the previous code sets [3], [45].

Fig. 5 shows the scatterplots of the simulation and LANL/MPA data extracted in the way described in 5. Fig. 5(a)–(c) shows P_{SIM} versus Pe, N_{SIM} versus Ne, and T_{SIM} versus Te, respectively. We can see the same characteristics as the results of the previous code set. P_{SIM} shows good correlation with Pe, while N_{SIM} is much higher than Ne, which is almost 1.0 [cm^{-3}]; therefore, T_{SIM} is estimated to be much smaller than the observed Te. The dotted line in Fig. 5(a) shows the regression line between P_{SIM} and Pe with a correlation coefficient of almost 0.53. The dotted line in Fig. 5(b) shows the Ne = 1.0 line, around which all data points are distributed.

In Fig. 5(c), T_{SIM-e}, the temperature estimated from P_{SIM} in the way described in 7, versus Te is plotted by magenta asterisks. It shows that the distribution is more aligned with the line of T_{SIM} = Te. To confirm this point quantitatively, we calculate Δ = sqrt (RSS/n), where RSS is the residual sum of squares and n is the number of samples, for both the as-is group of simulated data (shown by black asterisks) and the group of the estimated data (shown by magenta asterisks). The value of Δ is 4.25 [keV] for "the as-is group (black),"

2006/02/15 LANL(L4) MPA & Global magnetosphere MHD simulation
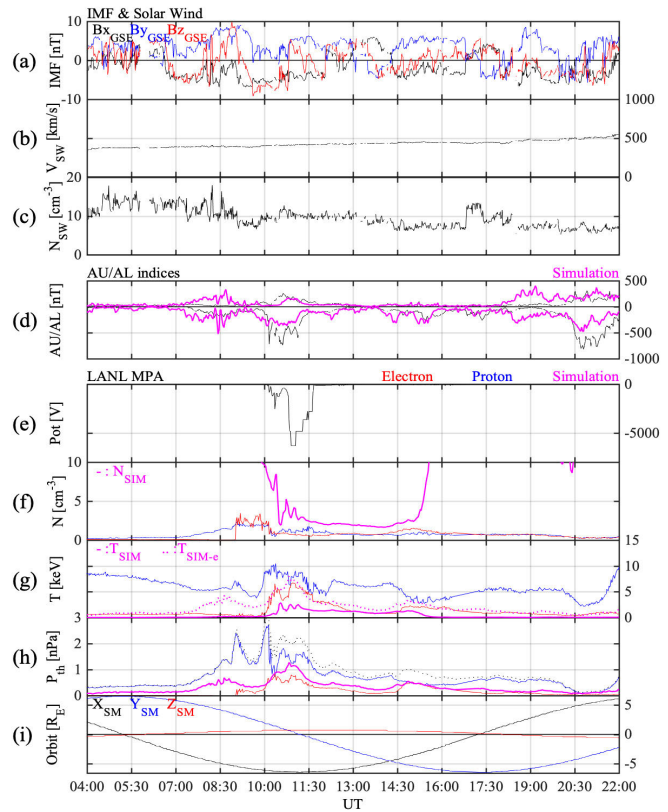

Fig. 4. LANL MPA and simulation data obtained using the improved magnetosphere MHD model on February 15, 2006. (a)–(d) Show the OMNI data, namely, (a) IMF, (b) solar wind speed, (c) solar wind density, and (d) AU/AL indices. (e)–(i) Show the LANL(L4) MPA data, namely, (e) satellite potential, (f) electron and ion densities (Ne and Ni, respectively), (g) temperatures (Te and Ti), (h) thermal pressures (Pe and Pi), and (i) spacecraft orbit. Magenta lines in (d) and (f)–(h) show the simulation data. The OMNI and LANL MPA data are provided by CDAWeb (https://cdaweb.gsfc.nasa.gov).

and 1.71 [keV] for "the estimated group (magenta)." Next, we calculate the ratios of residual to Te of each data point. We find that its average is 0.80 for "the as-is group (black)," and 0.18 for "the estimated group (magenta)." T_{SIM-e} is also plotted in Fig. 4(g) by the magenta dotted line. It can be seen that T_{SIM-e} traces Te much better than T_{SIM}.

Summarizing the above, it is confirmed that the estimation method for Ne, Ni, Te, and Ti described in 7 can be applied to the output of the real-time simulation currently in operation. Looking carefully at Fig. 5(a) and (c), P_{SIM} tends to be slightly higher than Pe, and T_{SIM-e} is distributed above the line of T_{SIM} = Te. Therefore, it may be possible to further modify T_{SIM} by multiplying a certain factor, in addition to the modification of T_{SIM} assuming Ne = 1.0 [cm^{-3}]. However, we adopt the present estimation method here for simplicity.

VII. QUICK ESTIMATION METHOD FOR EQUILIBRIUM SURFACE POTENTIAL

Generally, the charging calculation by the spacecraft charging models takes hours or days for one space environment condition. Therefore, even if plasma data are provided in real time, it is impossible to obtain satellite potentials in real
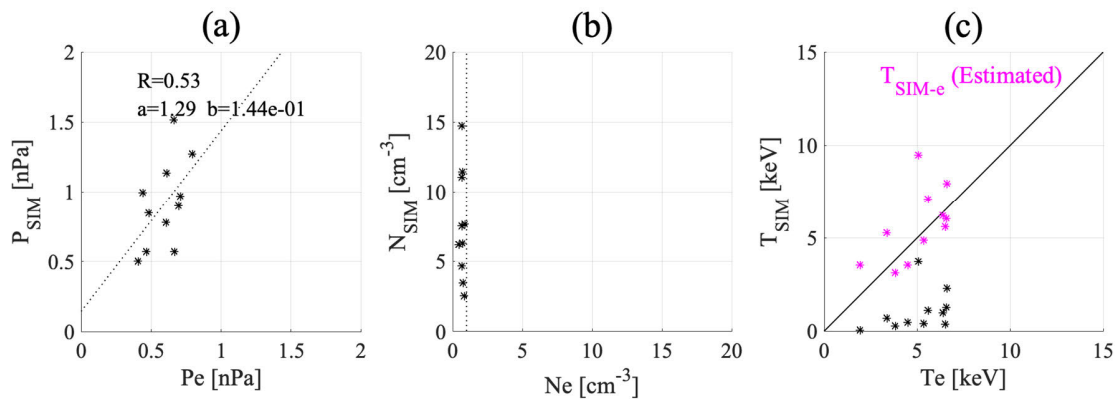
Fig. 5. Scatterplot of LANL MPA and simulation data obtained using the improved magnetosphere MHD model. (a) Simulated pressure P_{SIM} versus electron pressure Pe. (b) Simulated density N_{SIM} versus electron density Ne. (c) Simulated temperature T_{SIM} versus electron temperature Te. In (c), T_{SIM-e}, the estimated temperature assuming $N_{SIM} = 1.0$ [cm^{-3}], is plotted by magenta asterisks. The dotted line in (a) is the regression line between P_{SIM} and Pe. The dotted line in (b) is the Ne = 1.0 line.

time. To overcome this problem, we have developed a quick estimation method for the equilibrium surface potential using SPIS.

First, we predesign a model satellite on SPIS, as shown in Section IV. Next, we calculate the equilibrium floating potentials in advance for many combinations of input parameters for SPIS. We fit polynomial functions to the precalculation data. Using the obtained functions, we can instantaneously estimate the equilibrium surface potentials of the model satellite for any given set of input parameters.

As noted in Section IV, SPIS can accept both single-Maxwellian and double-Maxwellian distributions as plasma environments. The number of input parameters, in other words, the independent variables of the precalculation and fitting, are four and eight for the single- and double-Maxwellian assumptions, respectively. Therefore, whereas in principle the above method is feasible, the precalculation becomes very extensive and the fitting becomes a very complex problem.

In this study, we derive from the magnetosphere MHD simulation data the representative values of Ne, Ni, Te, and Ti for keV plasmas, assuming that the environmental plasma is in a single-Maxwellian distribution. Even with the single-Maxwellian assumption, there are still four input parameters (independent variables) (Ne, Te, Ni, and Ti), and the precalculation is still very extensive. In this study, however, the problem can be simplified to one with only one independent variable, Te, by assuming Ne = Ni = 1 [cm^{-3}] and Ti = 1.9 × Te, as shown in the previous section.

Fig. 6 shows the precalculation data for the model satellite (the Michibiki-1 satellite). The potential of the frame (satellite body and all parts grounded to it) and the maximum solar panel potential at equilibrium for both the eclipse and sunlit conditions are shown as functions of Te. Polynomial functions are fit to the precalculation data of frame and maximum potentials, respectively. See [46] for details. Using these functions, we can instantaneously obtain the equilibrium frame and maximum potentials of the model satellite for both the eclipse and sunlit conditions for any value of Te. As the absolute value of the difference between the frame and maximum potentials, we can also instantaneously obtain the

differential potential, probably the most important information for the surface charging/discharging risk. Fig. 7 shows an example of the surface potential distribution for the model satellite (the Michibiki-1 satellite) obtained by the charging calculation for Te = 32.0 [keV], Ne = Ni = 1.0 [/cm^3], and Ti = 1.9 Te [keV]. Fig. 7(a) and (b) shows the surface potential for the eclipse and sunlit conditions, respectively. The differential potential is maximized between the frame and a mesh of solar cell surfaces far from the satellite body, where the ESD is most likely to occur. Note that if an ESD occurs between the solar cell and its paddle plate (which is equipotential to the frame), it could lead to a satellite failure.

VIII. SURFACE CHARGING ASSESSMENT SYSTEM

Based on the method of estimating the input parameters for SPIS from the MHD simulation data and the quick estimation method for equilibrium surface potentials by using SPIS, we developed a surface charging assessment system for the GEO region. In 2021, we upgraded the system from the prototype version reported in [3], and we released the new website at the end of June 2022 (https://secures.nict.go.jp).

Fig. 8 shows a snapshot of the web page. The outline is as follows.

1) The bottom two images show the simulated plasma pressure distribution on the geomagnetic equatorial plane and 6.6-R_E sphere. The image of the 6.6-R_E sphere is shown in the geographic coordinate system.
2) The data are extracted every 5 min from the real-time magnetosphere MHD simulation running on the HPC system at NICT.
3) A three-axis stabilized satellite is assumed as the model satellite (see Section IV).
4) When users specify an arbitrary location on the image of the 6.6-R_E sphere, the plasma parameters (simulation output), information on sunlit or eclipse condition (shown as 0 or 1), and equilibrium satellite surface potentials (the maximum values of the surface potential, frame potential, and differential potential) for those conditions at that location are instantaneously displayed in Table I.

This article has been accepted for inclusion in a future issue of this journal. Content is final as presented, with the exception of pagination.

NAKAMIZO et al.: DEVELOPMENT OF A SURFACE CHARGING ASSESSMENT SYSTEM FOR THE GEO REGION 7
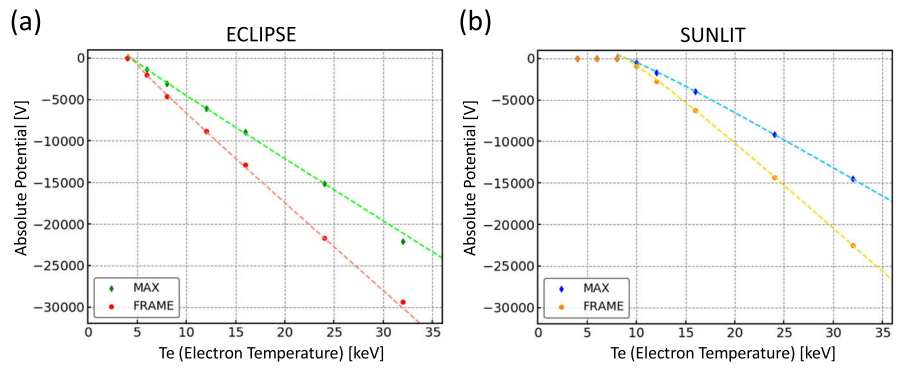

Fig. 6. Surface potentials of the model satellite (the Michibiki-1 satellite) calculated using SPIS. The frame potential and maximum solar panel potential of the model satellite (the Michibiki-1 satellite) at equilibrium were calculated using SPIS. (a) Data for the eclipse condition. (b) Data for the sunlit condition. The polynomial functions are fit to the precalculation data of frame and maximum potentials.
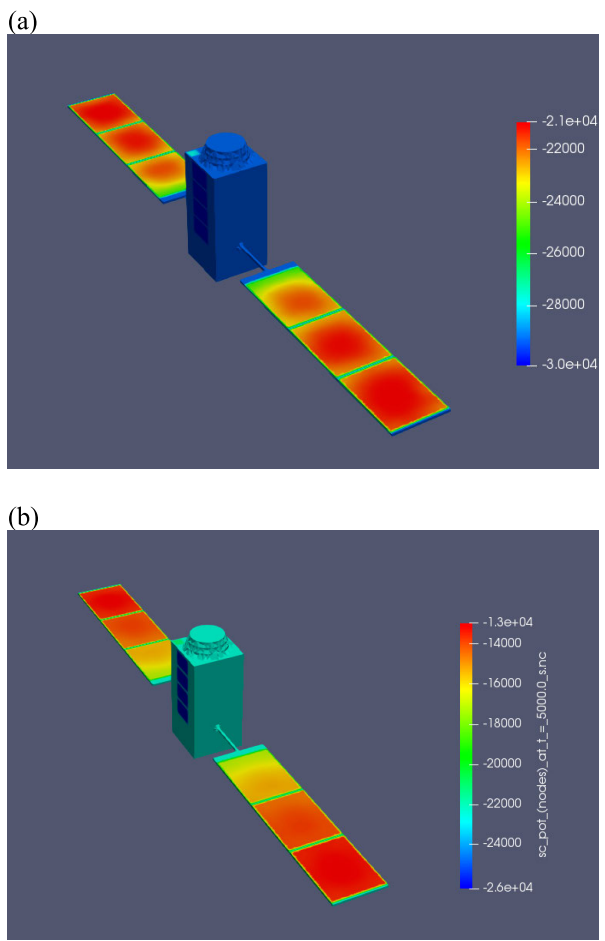

Fig. 7. Example of the surface potential distribution for the model satellite obtained by the charging calculation using SPIS for Te = 32.0 [keV], Ne = Ni = 1.0 [/cm^3], and Ti = 1.9 Te [keV]. (a) For the eclipse condition. (b) For the sunlit condition.
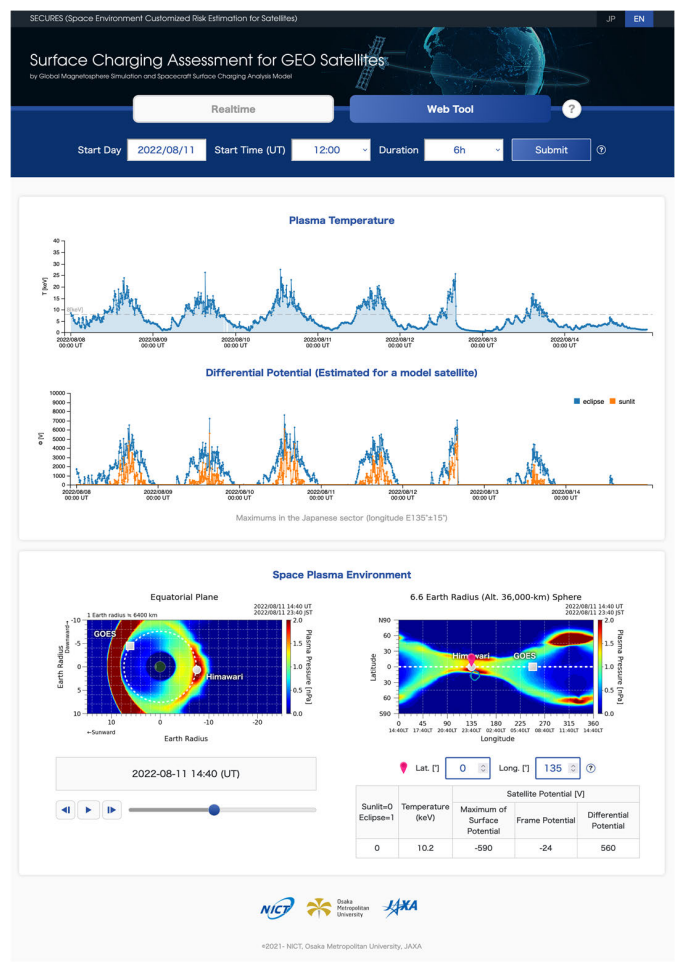

Fig. 8. New web page of the surface charging estimation system for the GEO region using global magnetosphere MHD model and SPIS.

5) The users can specify the location of interest by moving the pin on the image or inputting the longitude and latitude.

6) The upper two plots show the time series of the $T_{\text{SIM-e}}$ maximum and the corresponding differential potential for both sunlit and eclipse conditions for the GEO region in the Japanese sector (longitude = E135° ± 15° and latitude = 0° ± 10°). These plots can be used as a reference for the worst-case scenario for the Japanese sector.

7) The "Realtime" page shows the latest condition. The "Web Tool" page provides the past data. On the "Web Tool" page, users can specify the date, start time (UT), and duration according to their interests.

This article has been accepted for inclusion in a future issue of this journal. Content is final as presented, with the exception of pagination.

8   IEEE TRANSACTIONS ON PLASMA SCIENCE

8) The average propagation time of the solar wind from the L1 point to the front of the Earth's magnetosphere is about 1 h, and the sum of the processing times of the real-time simulation system and the surface charging assessment system is about 20 min. Therefore, the lead time of the "Realtime" page is about 40 min.

IX. SUMMARY AND DISCUSSION

For the safety and stability of satellite operations, we have been conducting the satellite charging estimation project SECURES [3]. The approach of SECURES is to combine the space environment and spacecraft charging models. In SECURES-Surface Charging, we use a global magnetosphere MHD model as the environment model, and we target the GEO region as the first step of charging estimation. To perform the magnetosphere simulation under realistic conditions, we improved the model by introducing the effects of the tilt and precession of the dipole axis of the Earth's magnetic field [39]. With this improvement, the magnetosphere MHD model could be ready for operational use. In combining the magnetosphere MHD model and spacecraft charging models, we encountered two challenges and took the following approaches to overcome them.

1) The spacecraft charging models require the densities and temperatures of electrons and ions as their inputs. However, the magnetosphere MHD model does not provide the electron and ion parameters separately. By comparing the LANL/MPA and MHD simulation data, we found that the simulated plasma pressure is in good agreement with the observed electron pressure, whereas the simulated density is much higher than the observed electron density, which is almost 1.0 [cm^{-3}], and the simulated temperature is lower than the observed electron temperature. Based on these characteristics, we developed a method of deriving the representative values for the keV plasmas used as the input parameters for the charging models from the simulation output for the GEO region.

2) The other problem is that the charging calculation takes a long time; therefore, even if the plasma dataset is provided in real time, it is impossible to obtain satellite potentials in real time. Thus, we developed a method of quickly estimating the satellite surface potentials by precalculation analysis using SPIS.

Based on (1) and (2), we combined the magnetosphere MHD model and SPIS and developed a surface charging assessment system for a model satellite in the GEO region, which operates in real time.

The surface charging is caused by: 1) space plasmas (electrons and ions) surrounding the spacecraft that flow into and away from the spacecraft's surface; 2) photoelectrons emitted from the spacecraft due to sunlight; and 3) secondary electrons and backscattered electrons by inflowing space plasmas that escape from the spacecraft surface. The equilibrium surface potential is determined relative to the surrounding plasmas when the net current generated by (1)–(3) is zero (see [47]).

In the GEO region, there are both cold (<100 [eV]) and hot (∼keV) plasmas. Therefore, charged particles contributing to the surface charging in the GEO region basically consist of these multicomponent electrons and ions. Moreover, the population of hot plasmas injected into the near-Earth region is known to be better fit by the double (or more)-Maxwellian than by the single-Maxwellian (see [48], [49], [50]), and it is suggested that the severe environment in the GEO region is better represented by the triple-Maxwellian or Kappa distribution (see [14]). Moreover, the occurrence of surface charging is distributed from around midnight, where substorm injection occurs, to the early-morning sectors [8], [9], [10], [11], indicating that the injected electrons drift eastward and cause the surface charging there.

On another subject, it has been known that the electron temperature is the most influential parameter for surface charging and that high-level surface charging starts to occur when the electron temperature exceeds a critical threshold (see [51]). For example, Olsen [52] showed for the Spacecraft Charging At High Altitudes (SCATHA) spacecraft that surface charging occurs when electron fluxes extend above 10 keV. Thomsen et al. [53] showed for the LANL MPA data that the charging will occur for the electron fluxes that extend above 8 keV. Mateìo-Veìlez et al. [14], using the LANL MPA data selected by several criteria, showed that the negative surface potential in the GEO region was developed by the increase of 10–50-keV electron flux.

The global magnetosphere MHD model (one of which we use as the environment model) solves the time evolution of macroscopic quantities, i.e., moments derived in principle by integrating the distribution function, and a single-Maxwellian distribution is implicitly assumed in the MHD approximation. Thus, it does not distinguish and perfectly include the contributions of cold, hot, and higher components in the distribution function, and it does not also distinguish ions and electrons.

First, we consider the effect of omitting the cold plasmas on charging estimation. In the case where a satellite is charged below minus several hundred volts under multitemperature component (cold and hot) plasma, applying the orbital motion limited (OML) theory [54], cold electrons are mostly reflected due to the negative potential and do not contribute to further negative charging. On the other hand, cold ions are attracted to the satellite due to the negative potential. The lower the temperature, the more the ions work to suppress the negative surface charging. Therefore, omitting the cold plasmas, as in this study, may overestimate the negative surface potential. However, the severe surface charging on the order of kV is caused by a sufficient amount of electron flux such as several–several tens of keV, as described above. By using the magnetosphere MHD models, we can derive the representative values of electron temperature and other parameters for keV plasmas. Therefore, although our charging estimation scheme does not include the effect of suppression by cold ions, it is considered to provide a practical first approximation for severe surface charging.

Next, we consider the situation where the ambient plasma is better fit by a double (or more)-Maxwellian or Kappa distribution. In such cases, the high-energy part of the distribution and its contribution to surface charging is likely underestimated in our estimation. Therefore, in such cases, the negative surface

This article has been accepted for inclusion in a future issue of this journal. Content is final as presented, with the exception of pagination.

NAKAMIZO et al.: DEVELOPMENT OF A SURFACE CHARGING ASSESSMENT SYSTEM FOR THE GEO REGION 9

potential may be underestimated in our method. However, with the single-Maxwellian assumption at present, we can derive from the MHD simulation data the most influential parameter, the electron temperature, and others.

As a conclusion, our product should be useful to some extent for surface charging estimation although it is at present not perfect due to the simplification related to the characteristics of the MHD model. Importantly, we have achieved real-time surface charging estimation tailored to a model satellite and its information dissemination as the first step, fully on the basis of physics-based models by realizing the real-time magnetosphere MHD simulation and developing the quick estimation method for equilibrium surface potentials using SPIS. To achieve advanced charging estimation, it is necessary to provide more detailed descriptions of the charged particle environments. One effective way to do this is to use inner magnetosphere models such as those described in [18], [19], [20], and [21]. These models can also be used to estimate internal charging, which is the target of SECURES, too. These are our future challenges.

On the other hand, although the inner magnetosphere models (see [18], [19], [20]) can describe the behavior of charged particles, they require the external boundary conditions to perform the simulations. In most cases, one of them is the electric field at the high-latitude boundary of the ionosphere or the distribution of large-scale FAC in the high-latitude ionosphere, the so-called Region 1 FAC [55] driven by the solar wind–magnetosphere interaction. Either of them is used as the input to calculate the electric field throughout the ionosphere, and the calculated electric field is mapped to the magnetosphere to calculate the particle behavior at the next time step. Another necessary boundary condition is the distribution of plasmas at the outer boundary of the magnetosphere, which are the source particles in the simulation. These boundary conditions are given observationally or by the magnetosphere MHD models (see [28], [29], [30], [56]). This means that we need the magnetosphere MHD model, even if we use inner magnetosphere models, to simulate the plasma environment from the solar wind and IMF inputs on a first principle basis without any observational assumptions. Moreover, substorm injection, the major cause of surface charging, is a localized and temporal phenomenon. The location and timing of its occurrence vary from event to event. (The location is generally in the premidnight sector.) As exemplified by the case of the Galaxy 15 spacecraft [57], we need to predict the location and timing of substorm injection. That is, we need to predict the time development of the near-Earth space during substorms. Among the physics-based models, only the magnetosphere MHD model can simulate the substorm dynamics.

But is its reproducibility sufficient? As demonstrated using available observational data, our global MHD model reasonably reproduces the plasma pressure although the breakdown of density and temperature remains incomplete. Additionally, it performs well in reproducing the AU/AL indices, which are indicators of substorm activities. Therefore, the model captures the force balance and its development in the magnetosphere, as well as substorm processes, on a global scale. However, we do not believe that the MHD model precisely reproduces

the timing, location, and intensity of substorm injections. To address this limitation, in our charging estimation product shown in Fig. 8, we examine the worst values of plasma parameter within a region a dozen degrees wide from the target point (in this case, 135°E longitude and 0° latitude over Japan). We derive satellite potentials using these values and display them as reference values. To enhance the global MHD model's reproducibility, data assimilation would be an effective approach, but it requires rich observational data, including keV-plasma moment data, and it is our future work. As for enhancing the reproducibility of the physical process itself, the description of the magnetosphere–ionosphere coupling process (as conventionally presented in Section II) can serve as a crucial factor for model improvement [58], [59], [60] because it has been demonstrated that the ionosphere actively influences magnetospheric configuration and dynamics, including substorms [61], [62], [63].

References

[1] D. C. Ferguson, S. P. Worden, and D. E. Hastings, "The space weather threat to situational awareness, communications, and positioning systems," *IEEE Trans. Plasma Sci.*, vol. 43, no. 9, pp. 3086–3098, Sep. 2015, doi: 10.1109/TPS.2015.2412775.

[2] J. C. Green, J. Likar, and Y. Shprits, "Impact of space weather on the satellite industry," *Space Weather*, vol. 15, no. 6, pp. 804–818, Jun. 2017, doi: 10.1002/2017SW001646.

[3] T. Nagatsuma et al., "Development of space environment customized risk estimation for satellites (SECURES)," *Earth Planets Space*, vol. 73, no. 26, pp. 1–14, Jan. 2021, doi: 10.1186/s40623-021-01355-x.

[4] J.-F. Roussel et al., "SPIS open-source code: Methods, capabilities, achievements, and prospects," *IEEE Trans. Plasma Sci.*, vol. 36, no. 5, pp. 2360–2368, Oct. 2008, doi: 10.1109/TPS.2008.2002327.

[5] T. Muranaka et al., "Development of multi-utility spacecraft charging analysis tool (MUSCAT)," *IEEE Trans. Plasma Sci.*, vol. 36, no. 5, pp. 2336–2349, Oct. 2008, doi: 10.1109/TPS.2008.2003974.

[6] S. Hosoda et al., "Laboratory experiments for code validation of multiutility spacecraft charging analysis tool (MUSCAT)," *IEEE Trans. Plasma Sci.*, vol. 36, no. 5, pp. 2350–2359, Oct. 2008, doi: 10.1109/TPS.2008.2003973.

[7] S. E. DeForest, "Spacecraft charging at synchronous orbit," *J. Geophys. Res.*, vol. 77, no. 4, pp. 651–659, Feb. 1972, doi: 10.1029/ja077i004p00651.

[8] H. E. Spence, J. B. Blake, and J. F. Fennell, "Surface charging analysis of high-inclination, high-altitude spacecraft: Identification and physics of the plasma source region," *IEEE Trans. Nucl. Sci.*, vol. 40, no. 6, pp. 1521–1524, Dec. 1993, doi: 10.1109/23.273510.

[9] T. P. O'Brien and C. L. Lemon, "Reanalysis of plasma measurements at geosynchronous orbit," *Space Weather*, vol. 5, no. 3, pp. 1–11, Mar. 2007, doi: 10.1029/2006sw000279.

[10] H. Choi et al., "Analysis of GEO spacecraft anomalies: Space weather relationships," *Space Weather*, vol. 9, no. 6, pp. 1–12, Jun. 2011, doi: 10.1029/2010SW000597.

[11] J. E. Mazur, J. F. Fennell, J. L. Roeder, P. T. O'Brien, T. B. Guild, and J. J. Likar, "The timescale of surface-charging events," *IEEE Trans. Plasma Sci.*, vol. 40, no. 2, pp. 237–245, Feb. 2012, doi: 10.1109/TPS.2011.2174656.

[12] M. H. Denton, M. F. Thomsen, H. Korth, S. Lynch, J. C. Zhang, and M. W. Liemohn, "Bulk plasma properties at geosynchronous orbit," *J. Geophys. Res., Space Phys.*, vol. 110, no. A7, pp. 1–17, Jul. 2005, doi: 10.1029/2004ja010861.

[13] M. F. Thomsen, M. H. Denton, B. Lavraud, and M. Bodeau, "Statistics of plasma fluxes at geosynchronous orbit over more than a full solar cycle," *Space Weather*, vol. 5, no. 3, pp. 1–9, Mar. 2007, doi: 10.1029/2006SW000257.

[14] J.-C. Matéo-Vélez, A. Sicard, D. Payan, N. Ganushkina, N. P. Meredith, and I. Sillanpää, "Spacecraft surface charging induced by severe environments at geosynchronous orbit," *Space Weather*, vol. 16, no. 1, pp. 89–106, Jan. 2018, doi: 10.1002/2017SW001689.

[15] N. Y. Ganushkina et al., "Worst-case severe environments for surface charging observed at LANL satellites as dependent on solar wind and geomagnetic conditions," *Space Weather*, vol. 19, no. 9, Sep. 2021, Art. no. e2021SW002732, doi: 10.1029/2021SW002732.

[16] M. H. Denton et al., "An empirical model of electron and ion fluxes derived from observations at geosynchronous orbit," *Space Weather*, vol. 13, no. 4, pp. 233–249, Apr. 2015, doi: 10.1002/2015SW001168.

[17] I. Sillanpää, N. Y. Ganushkina, S. Dubyagin, and J. V. Rodriguez, "Electron fluxes at geostationary orbit from GOES MAGED data," *Space Weather*, vol. 15, no. 12, pp. 1602–1614, Dec. 2017, doi: 10.1002/2017SW001698.

[18] R. A. Wolf, "Effects of ionospheric conductivity on convective flow of plasma in the magnetosphere," *J. Geophys. Res.*, vol. 75, no. 25, pp. 4677–4698, Sep. 1970, doi: 10.1029/JA075i025p04677.

[19] F. Toffoletto, S. Sazykin, R. Spiro, and R. Wolf, "Inner magnetospheric modeling with the Rice convection model," *Space Sci. Rev.*, vol. 107, no. 1, pp. 175–196, 2003, doi: 10.1023/a:1025532008047.

[20] V. K. Jordanova, J. U. Kozyra, A. F. Nagy, and G. V. Khazanov, "Kinetic model of the ring current-atmosphere interactions," *J. Geophys. Res., Space Phys.*, vol. 102, no. A7, pp. 14279–14291, Jan. 1997, doi: 10.1029/96ja03699.

[21] M.-C. Fok et al., "The comprehensive inner magnetosphere-ionosphere model l," *J. Geophys. Res. Space Phys.*, vol. 119, pp. 7522–7540, 2014, doi: 10.1002/2014JA020239.

[22] T. Ogino, "A three-dimensional MHD simulation of the interaction of the solar wind with the Earth's magnetosphere: The generation of field-aligned currents," *J. Geophys. Res., Space Phys.*, vol. 91, no. A6, pp. 6791–6806, Jun. 1986, doi: 10.1029/ja091ia06p06791.

[23] J. G. Lyon, J. A. Fedder, and C. M. Mobarry, "The Lyon–Fedder–Mobarry (LFM) global MHD magnetospheric simulation code," *J. Atmos. Solar-Terr. Phys.*, vol. 66, nos. 15–16, pp. 1333–1350, Oct. 2004, doi: 10.1016/j.jastp.2004.03.020.

[24] G. Tóth et al., "Space weather modeling framework: A new tool for the space science community," *J. Geophys. Res., Space Phys.*, vol. 110, no. A12, pp. 1–21, Dec. 2005, doi: 10.1029/2005ja011126.

[25] J. Raeder, D. Larson, W. Li, E. L. Kepko, and T. Fuller-Rowell, "OpenGGCM simulations for the THEMIS mission," *Space Sci. Rev.*, vol. 141, nos. 1–4, pp. 535–555, Dec. 2008, doi: 10.1007/s11214-008-9421-5.

[26] P. Janhunen et al., "The GUMICS-4 global MHD magnetosphere–ionosphere coupling simulation," *J. Atmos. Solar-Terr. Phys.*, vol. 80, pp. 48–59, May 2012, doi: 10.1016/j.jastp.2012.03.006.

[27] Y. Yu et al., "Initial results from the GEM challenge on the spacecraft surface charging environment," *Space Weather*, vol. 17, no. 2, pp. 299–312, Feb. 2019, doi: 10.1029/2018sw002031.

[28] Y. Yu, S. Su, J. Cao, V. K. Jordanova, and M. H. Denton, "Improved boundary conditions for coupled geospace models: An application in modeling spacecraft surface charging environment," *Space Weather*, vol. 20, no. 9, Sep. 2022, Art. no. e2022SW003178, doi: 10.1029/2022sw003178.

[29] V. Jordanova et al., "Specification of the near-Earth space environment with SHIELDS," *J. Atmos. Solar-Terr. Phys.*, vol. 177, pp. 148–159, Oct. 2018, doi: 10.1016/j.jastp.2017.11.006.

[30] V. K. Jordanova et al., "The RAM-SCB model and its applications to advance space weather forecasting," *Adv. Space Res.*, vol. 72, no. 12, pp. 5596–5606, Dec. 2023, doi: 10.1016/j.asr.2022.08.077.

[31] H. B. Garrett, "Review of quantitative models of the 0 to 100 keV near Earth plasma," *Rev. Geophys.*, vol. 17, no. 3, pp. 397–417, May 1979.

[32] T. Tanaka, "Substorm auroral dynamics reproduced by advanced global Magnetosphere-ionosphere (M–I) coupling simulation," in *Auroral Dynamics and Space Weather*, vol. 215, Y. Zhang and L. J. Paxton, Eds., Washington, DC, USA: AGU, Nov. 2015, pp. 177–190, doi: 10.1002/9781118978719.ch13.

[33] T. Tanaka, "Finite volume TVD scheme on an unstructured grid system for three-dimensional MHD simulation of inhomogeneous systems including strong background potential fields," *J. Comput. Phys.*, vol. 111, no. 2, pp. 381–389, Apr. 1994, doi: 10.1006/jcph.1994.1071.

[34] T. Moriguchi, A. Nakamizo, T. Tanaka, T. Obara, and H. Shimazu, "Current systems in the Jovian magnetosphere," *J. Geophys. Res., Space Phys.*, vol. 113, no. A5, pp. 1–10, May 2008, doi: 10.1029/2007ja012751.

[35] A. Nakamizo, T. Tanaka, Y. Kubo, S. Kamei, H. Shimazu, and H. Shinagawa, "Development of the 3-D MHD model of the solar corona-solar wind combining system," *J. Geophys. Res., Space Phys.*, vol. 114, no. A7, pp. 1–16, Jul. 2009, doi: 10.1029/2008ja013844.

[36] T. Tanaka et al., "Substorm convection and current system deduced from the global simulation," *J. Geophys. Res., Space Phys.*, vol. 115, no. A5, pp. 1–26, May 2010, doi: 10.1029/2009ja014676.

[37] K. Kitamura et al., "Properties of AE indices derived from real-time global simulation and their implications for solar wind-magnetosphere coupling," *J. Geophys. Res., Space Phys.*, vol. 113, no. A3, pp. 1–10, Feb. 2008, doi: 10.1029/2007ja012514.

[38] Y. Kubota et al., "Comparison of magnetospheric magnetic field variations at quasi-zenith orbit based on michibiki observation and REPPU global MHD simulation," *IEEE Trans. Plasma Sci.*, vol. 47, no. 8, pp. 3937–3941, Aug. 2019, doi: 10.1109/TPS.2019.2910301.

[39] A. Nakamizo, Y. Kubota, T. Nagatsuma, and T. Tanaka, "Near-Earth plasma environment and injection simulated by global magnetosphere model with precession of magnetic axis," presented at the JpGU—AGU Joint Meeting, Jul. 2020.

[40] Y. Kubota et al., "Study of IMF by dependence of plasma injection position using real-time magnetosphere simulation data," presented at the *Proc. JpGU—AGU Joint Meeting*, Jul. 2020.

[41] N. Inaba, A. Matsumoto, H. Hase, S. Kogure, M. Sawabe, and K. Terada, "Design concept of quasi zenith satellite system," *Acta Astronautica*, vol. 65, nos. 7–8, pp. 1068–1075, Oct. 2009, doi: 10.1016/j.actaastro.2009.03.068.

[42] H. Maeda, R. Kawachi, M. Nakamura, K. Koga, and H. Matsumoto, "Surface charging analysis of the quasi-zenith satellite 'MICHIBIKI,'" in *Proc. 15th Spacecraft Charging Technol. Conf.*, 2018, pp. 1–18.

[43] K. Toyoda and D. C. Ferguson, "Round-robin simulation for GEO worst-case environment for spacecraft charging," in *Proc. 13th Spacecraft Charging Technol. Conf.*, 2014, p. 171.

[44] M. Nakamura, S. Nakamura, R. Kawachi, and K. Toyoda, "Assessment of worst GEO plasma environmental models for spacecraft surface charging by SPIS," *Trans. Jpn. Soc. Aeronaut. Space Sci., Aerosp. Technol. Jpn*, vol. 16, no. 6, pp. 556–560, 2018, doi: 10.2322/tastj.16.556.

[45] M. Nakamura, "Forecast of the plasma environment in the geostationary orbit using the magnetospheric simulation," (in Japanese), *J. Plasma Fusion Res.*, vol. 88, pp. 83–86, 2012.

[46] M. Nakamura, A. Yamamoto, A. Nakamizo, and T. Nagatsuma, "Spacecraft surface charging estimation method around the geosynchronous altitude," in *Proc. 16th Spacecraft Charging Technol. Conf.*, 2022, pp. 1–18.

[47] H. B. Garrett, "The charging of spacecraft surfaces," *Rev. Geophys. Space Phys.*, vol. 19, no. 4, pp. 577–616, Nov. 1981, doi: 10.1029/RG019i004p00577.

[48] E. G. Mullen, M. S. Gussenhoven, and H. B. Garrett, "A worst case spacecraft environment as observed by SCATHA on 24 April 1979," Air Force Geophys. Lab., Hanscom AFB, MA, USA, Tech. Rep. AFGL-TR-81-0231, 1981.

[49] H. B. Garrett, D. C. Schwank, and S. E. Deforest, "A statistical analysis of the low-energy geosynchronous plasma environment–I. Electrons," *Planet. Space Sci.*, vol. 29, no. 10, pp. 1021–1044, Oct. 1981.

[50] H. B. Garrett, D. C. Schwank, and S. E. Deforest, "A statistical analysis of the low-energy geosynchronous plasma environment—II. Ions," *Planet. Space Sci.*, vol. 29, no. 10, pp. 1045–1060, Oct. 1981.

[51] S. T. Lai and M. Tautz, "High-level spacecraft charging in eclipse at geosynchronous altitudes: A statistical study," *J. Geophys. Res., Space Phys.*, vol. 111, no. A9, pp. 1–8, Sep. 2006, doi: 10.1029/2004ja010733.

[52] R. C. Olsen, "A threshold effect for spacecraft charging," *J. Geophys. Res., Space Phys.*, vol. 88, no. A1, pp. 493–499, Jan. 1983, doi: 10.1029/ja088ia01p00493.

[53] M. F. Thomsen, M. G. Henderson, and V. K. Jordanova, "Statistical properties of the surface-charging environment at geosynchronous orbit," *Space Weather*, vol. 11, no. 5, pp. 237–244, May 2013, doi: 10.1002/swe.20049.

[54] S. T. Lai, *Fundamentals of Spacecraft Charging: Spacecraft Interactions With Space Plasmas*. Princeton, NJ, USA: Princeton Univ. Press, 2012.

[55] T. Iijima and T. A. Potemra, "The amplitude distribution of field-aligned currents at northern high latitudes observed by triad," *J. Geophys. Res.*, vol. 81, no. 13, pp. 2165–2174, May 1976, doi: 10.1029/ja081i013p02165.

This article has been accepted for inclusion in a future issue of this journal. Content is final as presented, with the exception of pagination.

NAKAMIZO et al.: DEVELOPMENT OF A SURFACE CHARGING ASSESSMENT SYSTEM FOR THE GEO REGION 11

[56] A. Pembroke et al., "Initial results from a dynamic coupled magnetosphere-ionosphere-ring current model," *J. Geophys. Res., Space Phys.*, vol. 117, no. A2, pp. 1–21, Feb. 2012, doi: 10.1029/2011ja016979.

[57] T. M. Loto'aniu et al., "Space weather conditions during the Galaxy 15 spacecraft anomaly," *Space Weather*, vol. 13, no. 8, pp. 484–502, Aug. 2015, doi: 10.1002/2015sw001239.

[58] A. Yoshikawa et al., "Alfvenic-coupling algorithm for global and dynamical magnetosphere-ionosphere coupled system," *J. Geophys. Res., Space Phys.*, vol. 115, no. A4, pp. 1–7, Apr. 2010, doi: 10.1029/2009ja014924.

[59] A. Yoshikawa and R. Fujii, "Earth's ionosphere: Theory and phenomenology of cowling channels," in *Electric Currents in Geospace and Beyond* (Geophysical Monograph Series), vol. 235, A. Keiling, O. Marghit, and M. Wheatland, Eds., Hoboken, NJ, USA: Wiley, 2018, pp. 427–443, doi: 10.1002/9781119324522.ch25.

[60] A. Yoshikawa, O. Amm, H. Vanhamäki, A. Nakamizo, and R. Fujii, "Theory of cowling channel formation by reflection of shear Alfven waves from the auroral ionosphere," *J. Geophys. Res., Space Phys.*, vol. 118, no. 10, pp. 6416–6425, Oct. 2013, doi: 10.1002/jgra.50514.

[61] A. Yoshikawa, O. Amm, H. Vanhamäki, and R. Fujii, "Illustration of cowling channel coupling to the shear Alfven wave," *J. Geophys. Res., Space Phys.*, vol. 118, no. 10, pp. 6405–6415, Oct. 2013, doi: 10.1002/jgra.50513.

[62] A. Nakamizo, A. Yoshikawa, and T. Tanaka, "Study on effects of ionospheric polarization field and inner boundary conditions on magnetospheric dynamics and substorm processes in global MHD simulation," presented at the JpGU—AGU Joint Meeting, May 2017.

[63] A. Nakamizo and A. Yoshikawa, "Deformation of ionospheric potential pattern by ionospheric Hall polarization," *J. Geophys. Res., Space Phys.*, vol. 124, no. 9, pp. 7553–7580, Sep. 2019, doi: 10.1029/2018ja026013.
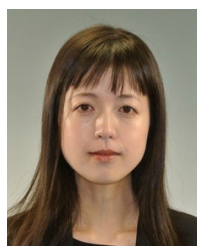
Yasubumi Kubota received the M.S. and Ph.D. degrees in science from the University of Tokyo, Tokyo, Japan, in 2004 and 2010, respectively.

In 2011, he joined the National Institute of Information and Communications Technology, Koganei, Japan, as a Researcher of space weather. Since 2021, he has been an Engineer of artificial intelligence with OMRON EXPERT ENGINEERING Corporation, Tokyo.

Kiyokazu Koga received the B.S. and M.S. degrees from the Department of Physics, Kyushu University, Fukuoka, Japan, in 1987 and 1989, respectively, and the Ph.D. degree from the Department of Earth and Planetary Sciences, Kyushu University, in 2016.

Since 1989, he has been with Japan Aerospace Exploration Agency, Tsukuba, Japan, where he is currently with the Space Environment Group, Research Unit 1, Research and Development Directorate. His research interests include spacecraft and space environment interactions, spacecraft charging, and the development of space environment measurement instruments.

Aoi Nakamizo received the M.S. and Ph.D. degrees in science from Kyushu University, Fukuoka, Japan, in 2002 and 2005, respectively.

She worked as a JST Researcher with Kyushu University. She worked with Nagoya University, Nagoya, Japan, and as a Senior Scientist with the Finnish Meteorological Institute, Helsinki, Finland. She joined the National Institute of Information and Communications Technology (NICT), Koganei, Japan, in 2014, and was assigned to the Radio Research Institute, in May 2015. Her work as a senior researcher involves the research and development of (real-time) magnetosphere simulations and space weather forecasting, as well as studies related to solar-terrestrial physics and magnetosphere–ionosphere coupling.

Masao Nakamura received the Ph.D. degree in science from Nagoya University, Nagoya, Japan, in 1997.

He is currently an Associate Professor with the Department of Aerospace Engineering, Osaka Metropolitan University, Osaka, Japan.

Haruhisa Matsumoto received the Bachelor of Engineering degree from the Shibaura Institute of Technology, Tokyo, Japan, in 1982.

He is currently with Japan Aerospace Exploration Agency, Tsukuba, Japan, focusing on space environment measurement and equipment development.

Tsutomu Nagatsuma received the M.Sc. and Ph.D. degrees in geophysics from Tohoku University, Sendai, Japan, in 1992 and 1995, respectively.

In 1995, he joined the Communications Research Laboratory (currently the National Institute of Information and Communications Technology), Koganei, Japan. He is an Executive Researcher with the Quantum ICT Collaboration Center, Koganei, and a Research Manager with the Space Environment Laboratory, Koganei. In addition, he is a Co-Chair of the Space Weather Coordination Group, Coordination Group for Meteorological Satellites. His research interests include solar wind–magnetosphere–ionosphere coupling, inner magnetosphere physics, and space weather forecast.

Dr. Nagatsuma is an Editor of *Progress in Earth and Planetary Science*.

Yoshizumi Miyoshi (Member, IEEE) received the M.S. and Ph.D. degrees in science from Tohoku University, Sendai, Japan, in 1998 and 2001, respectively.

He joined Nagoya University, Nagoya, Japan, as an Assistant Professor, in 2004, where he was promoted to Professor with the Institute for Space-Earth Environmental Research and the Graduate School of Engineering, in 2018. His research fields cover geospace system physics, including radiation belts, wave–particle interactions, and space weather forecast. He also works in space radiation environment on the Moon.